

## **Electronic Supporting Information for**

### **Nitrogen-doped carbon sponge derived from the self-assembly of poly(amic acid) for high performance oxygen reduction reaction**

Hui Sun<sup>\*a</sup>, Kai Jin<sup>a</sup>, Xiao Li<sup>a</sup>, Tian Wang<sup>\*b</sup> and Xiaoyong Lai<sup>\*a</sup>

<sup>a</sup>School of Chemistry and Chemical Engineering, State Key Laboratory of High-Efficiency Coal Utilization and Green Chemical Engineering, Ningxia University, Yinchuan 750021, China E-mail:  
[sunhui@nxu.edu.cn](mailto:sunhui@nxu.edu.cn), [xylai@nxu.edu.cn](mailto:xylai@nxu.edu.cn)

<sup>b</sup>Department of Chemistry, University of Washington, Seattle, WA 98195, United States E-mail:  
[twang91@uw.edu](mailto:twang91@uw.edu)

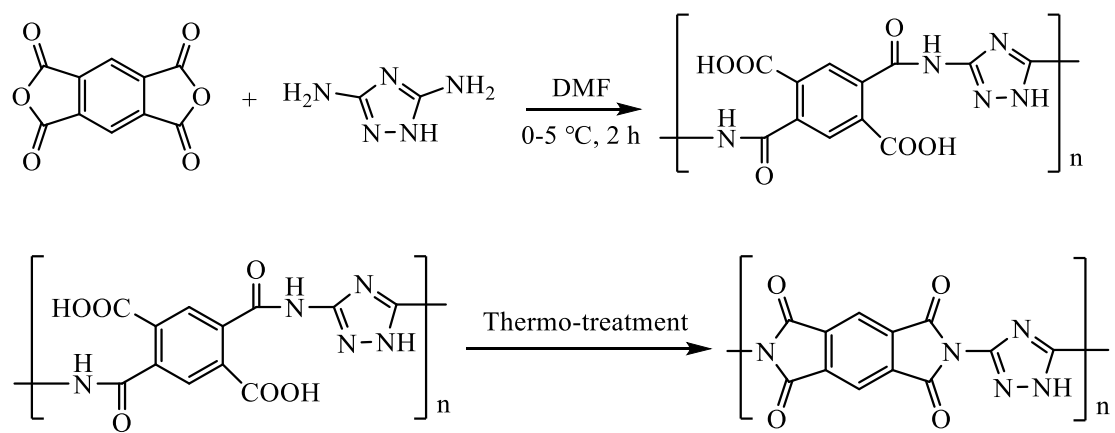


Fig. S1. Synthesis route of PAA and its thermo-induced cyclization reaction.

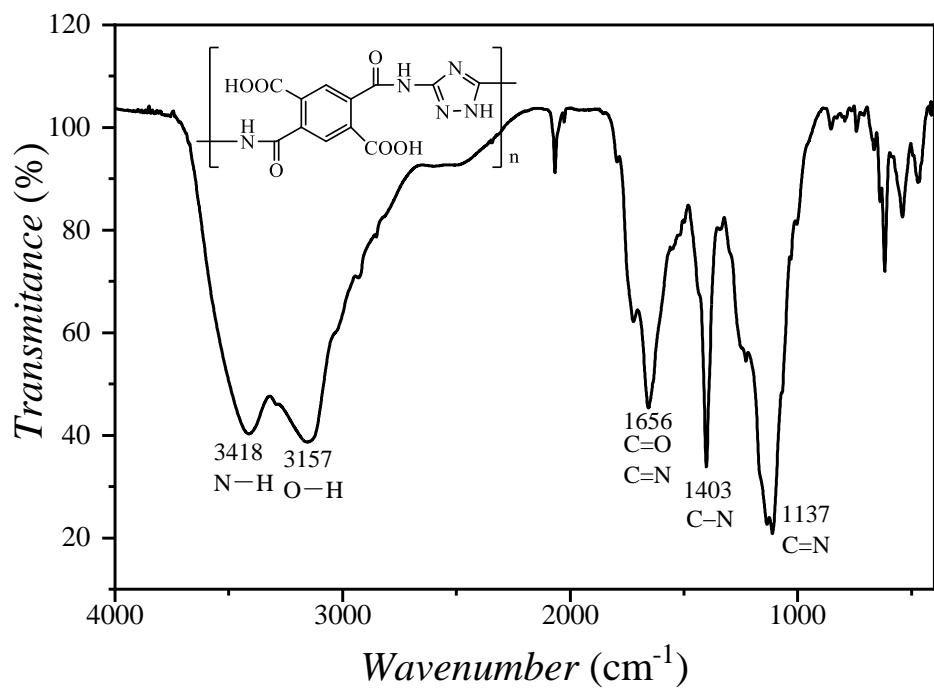


Fig. S2. FTIR spectrum of PAA.

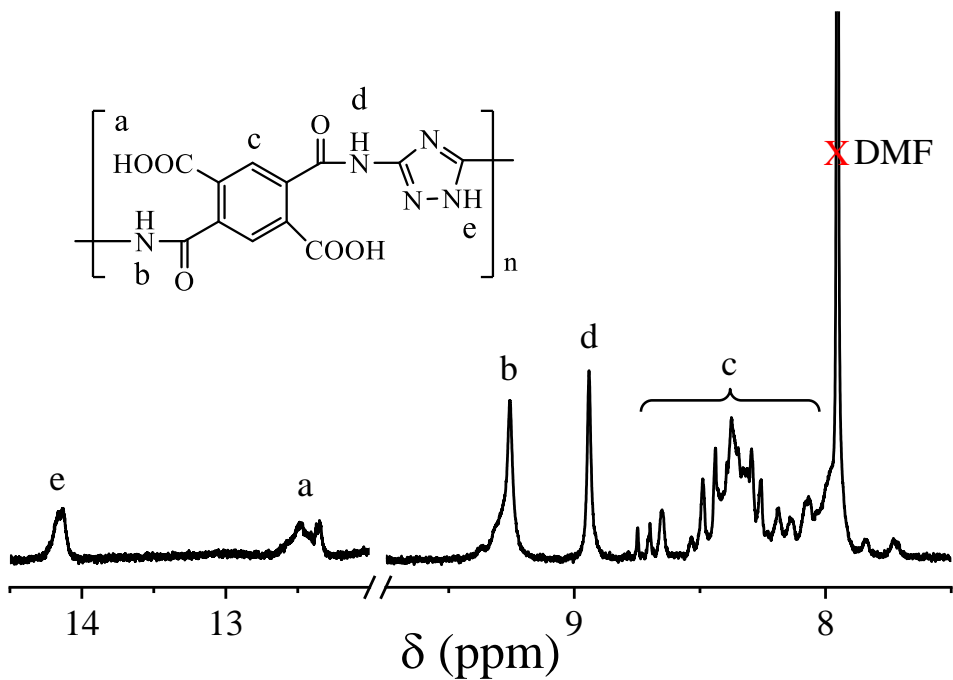


Fig. S3. <sup>1</sup>H NMR spectrum of PAA in  $\text{DMSO}-d_6$ .

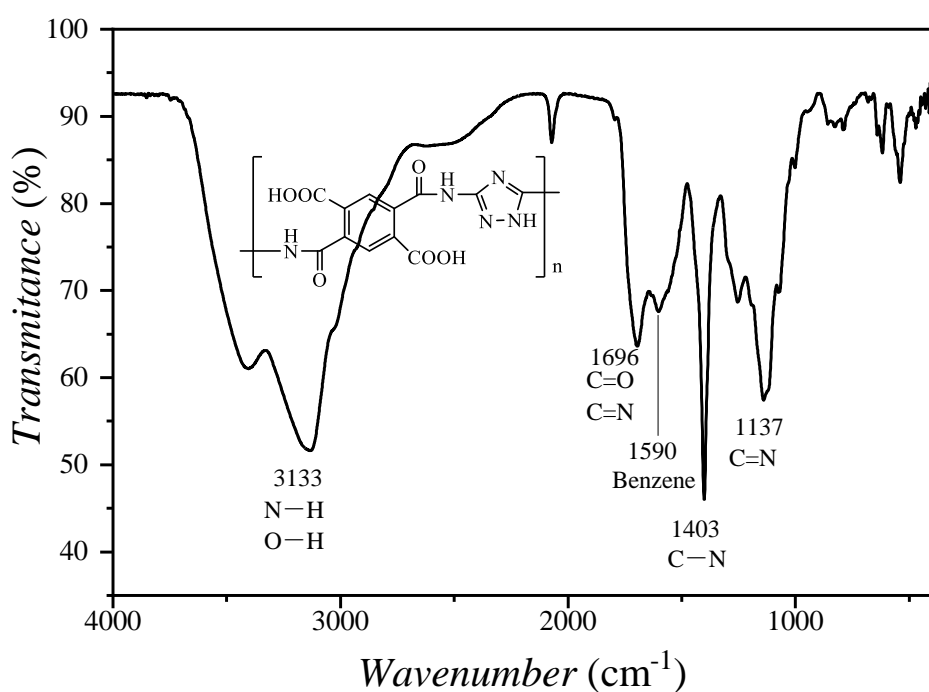


Fig. S4. FTIR spectrum of PAA sponge.

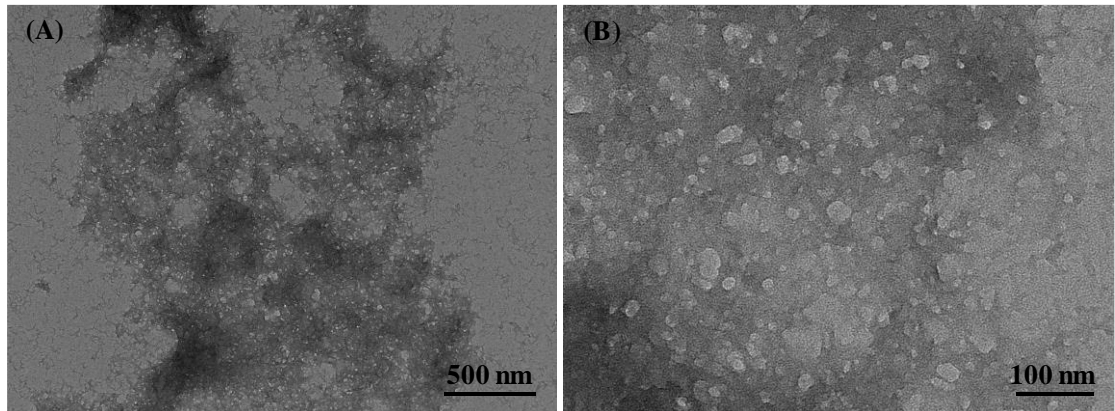


Fig. S5. (A) and (B) supplementary TEM images of PAA sponge at different magnifications.

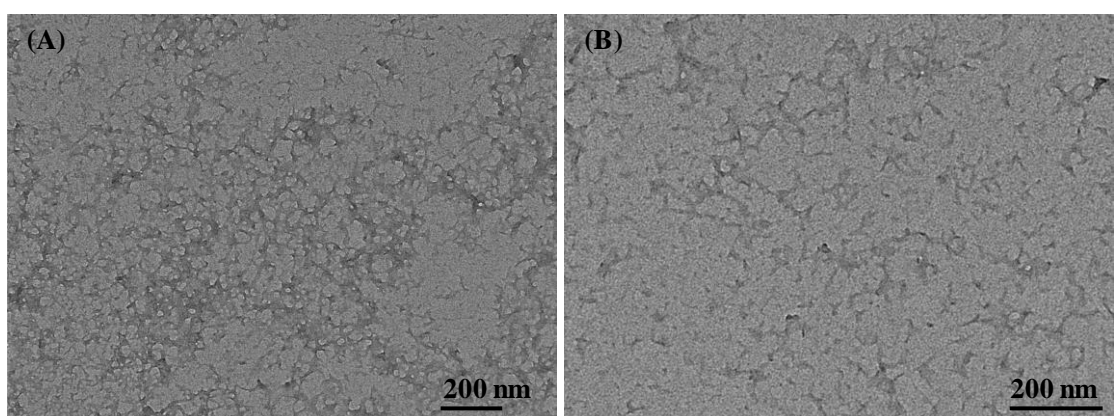


Fig. S6. (A) and (B) TEM images of PAA sponge at thin area and fragments of thin frameworks, respectively.

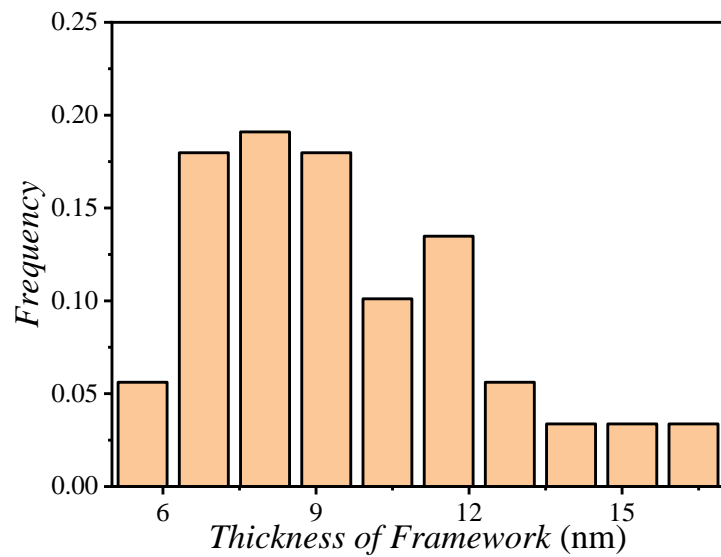


Fig. S7. Thickness of the framework of PAA sponge.

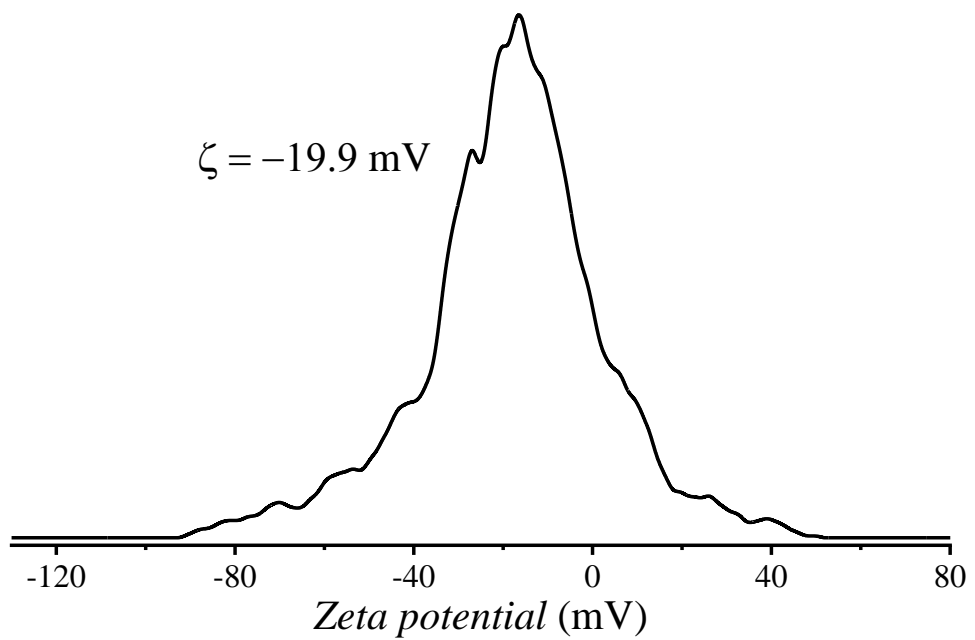


Fig. S8. Zeta potential of PAA sponge.

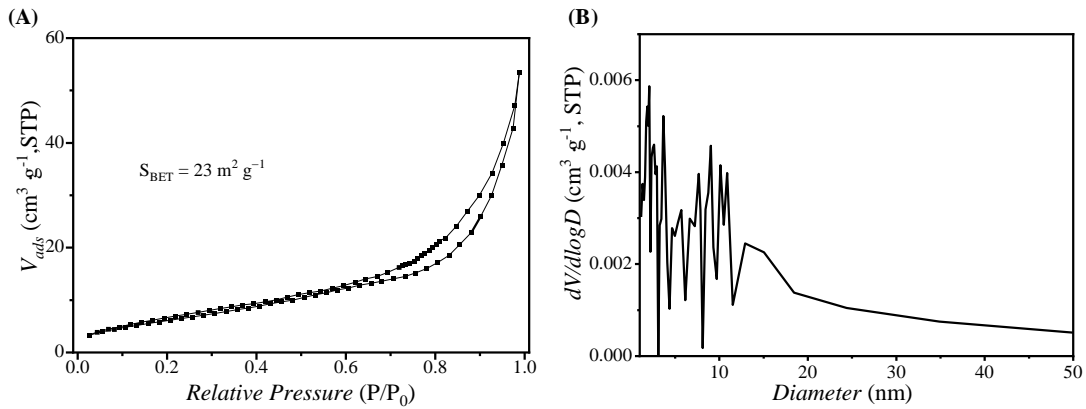


Fig. S9. (A) Nitrogen adsorption/desorption isotherm and (B) pore size distribution of PAA sponge.

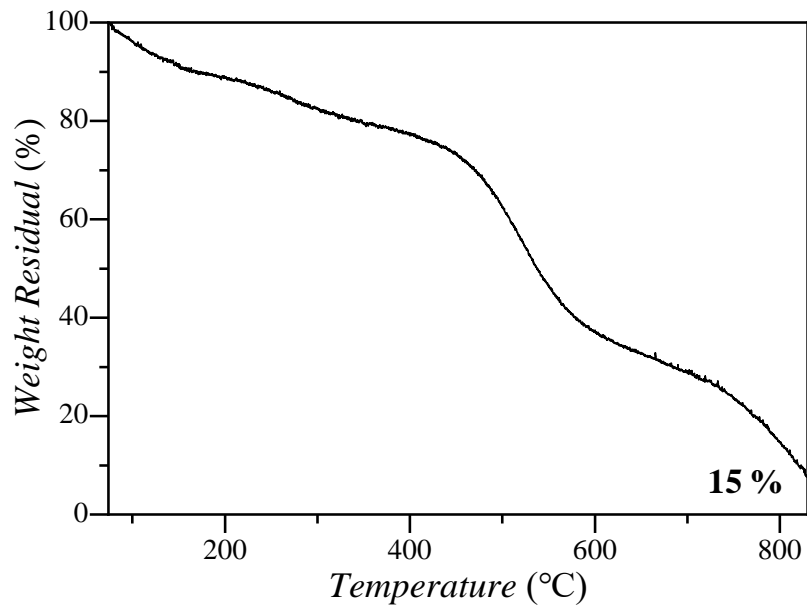


Fig. S10. TG curve of PAA sponge at nitrogen atmosphere.

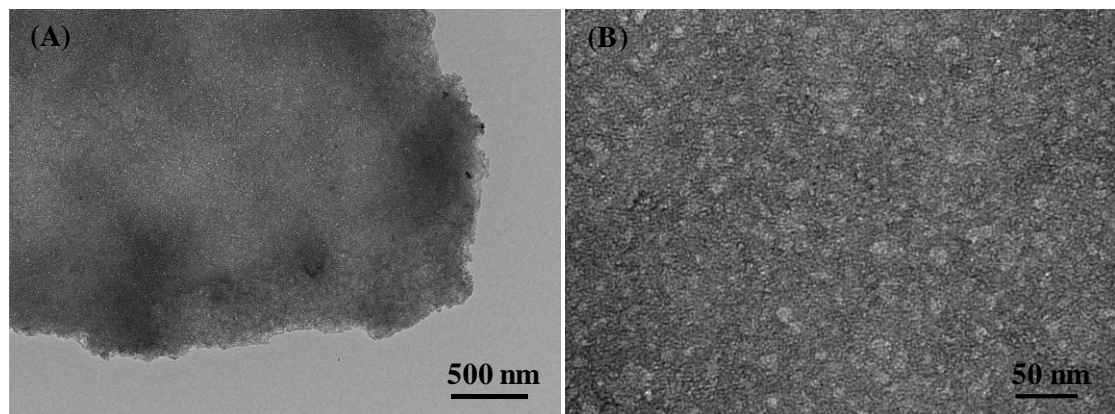


Fig. S11. (A) and (B) supplementary TEM images of NCS-800 at different magnifications.

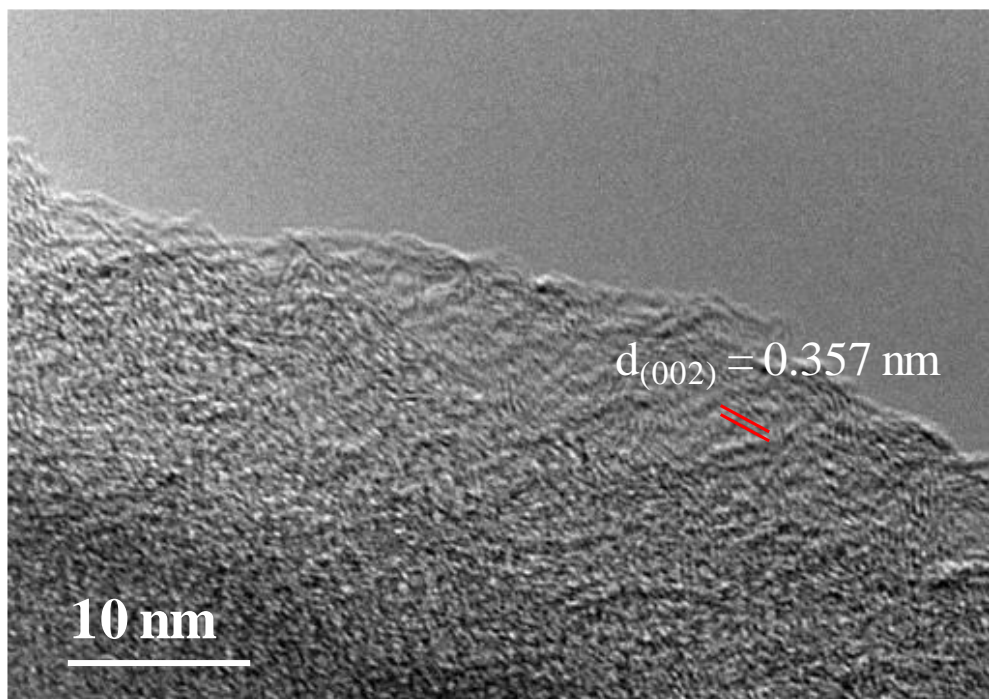


Fig. S12. HRTEM image of NCS-800.

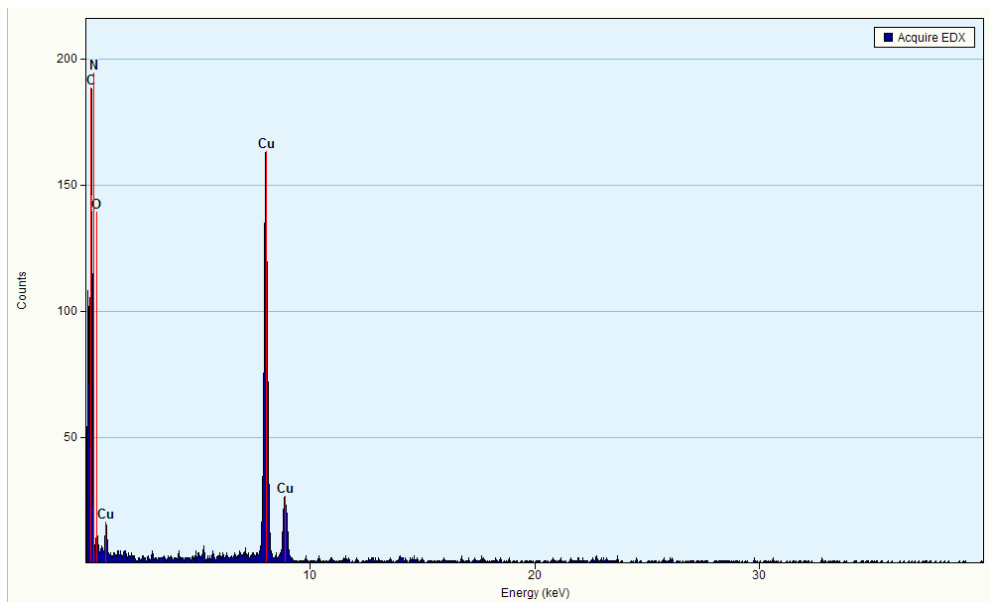


Fig. S13. EDS spectrum of NCS-800.

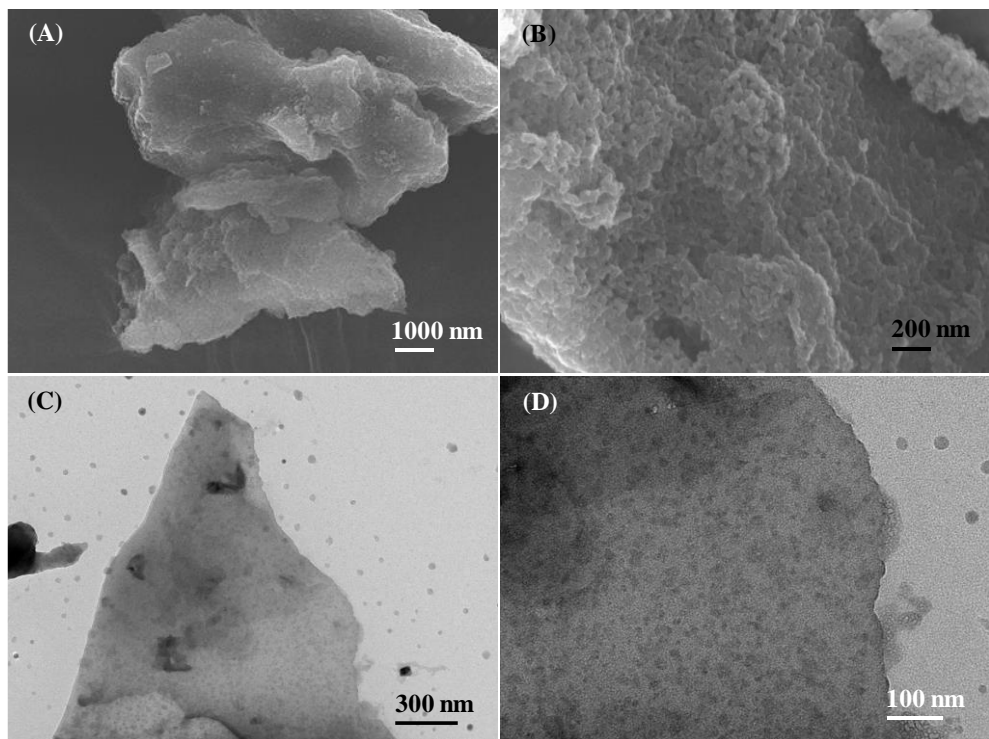


Fig. S14. (A), (B) SEM and (C), (D) TEM images of NCS-700.

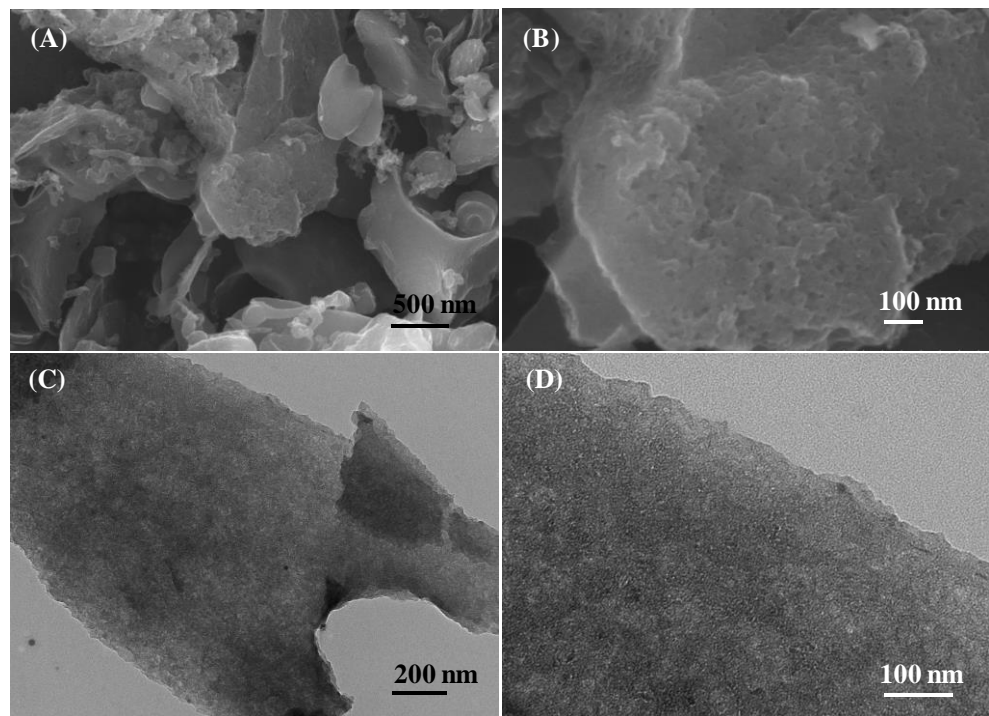


Fig. S15. (A), (B) SEM and (C), (D) TEM images of NCS-900.

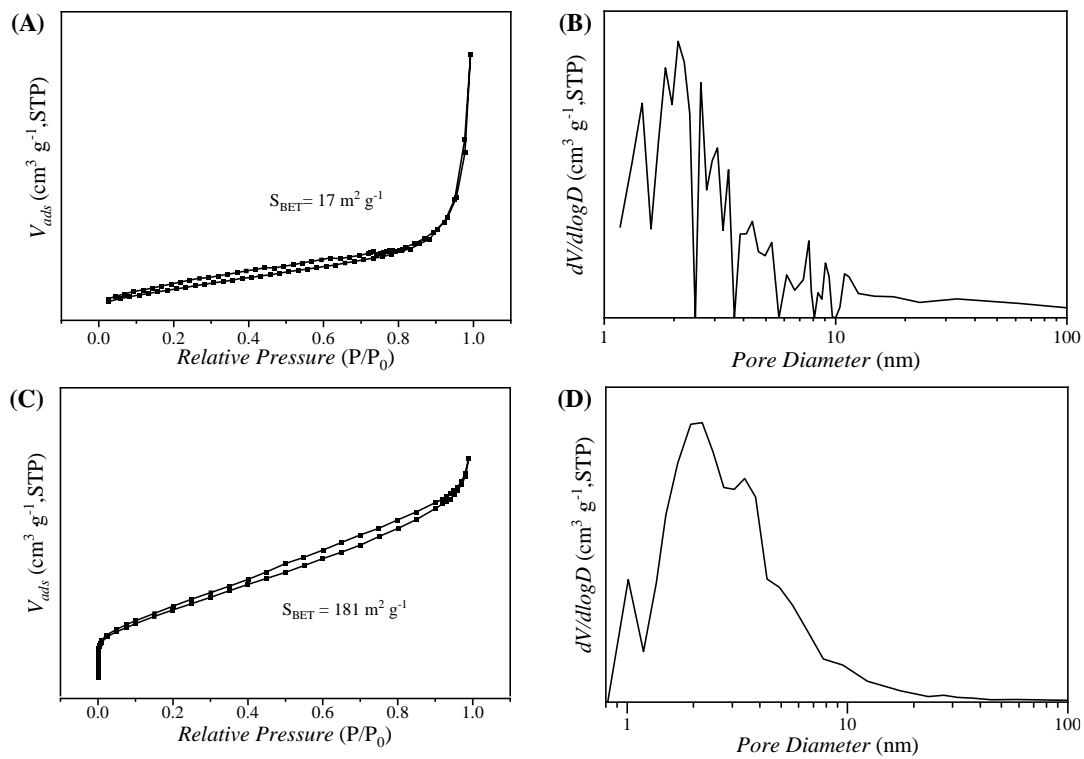


Fig. S16. Nitrogen adsorption/desorption isotherms and pore size distributions of (A), (B) NCS-700 and (C), (D) NCS-900, respectively.

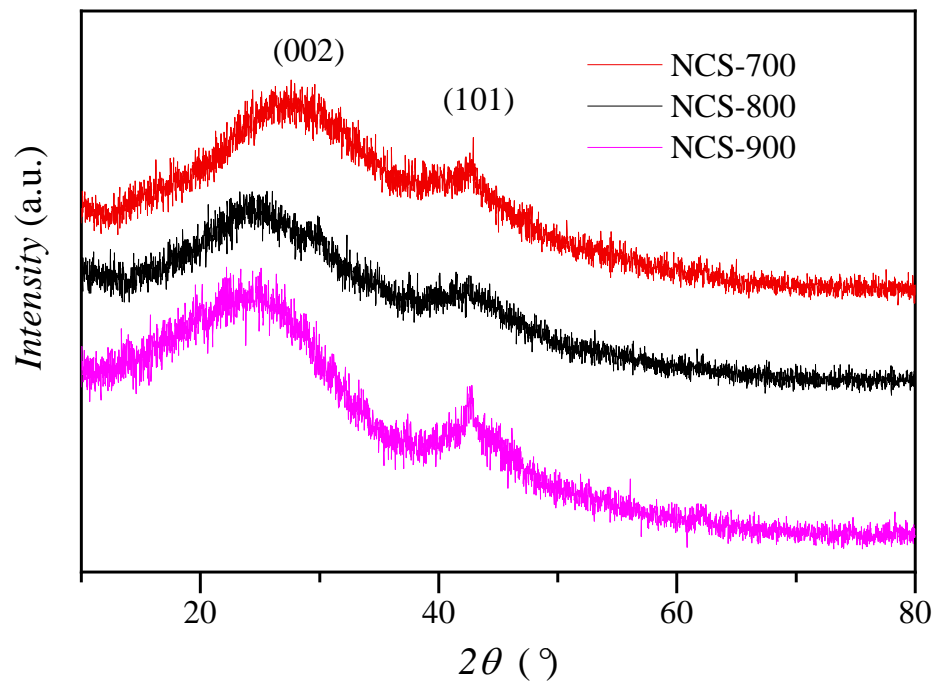


Fig. S17. XRD patterns of NCS-700, NCS-800 and NCS-900.

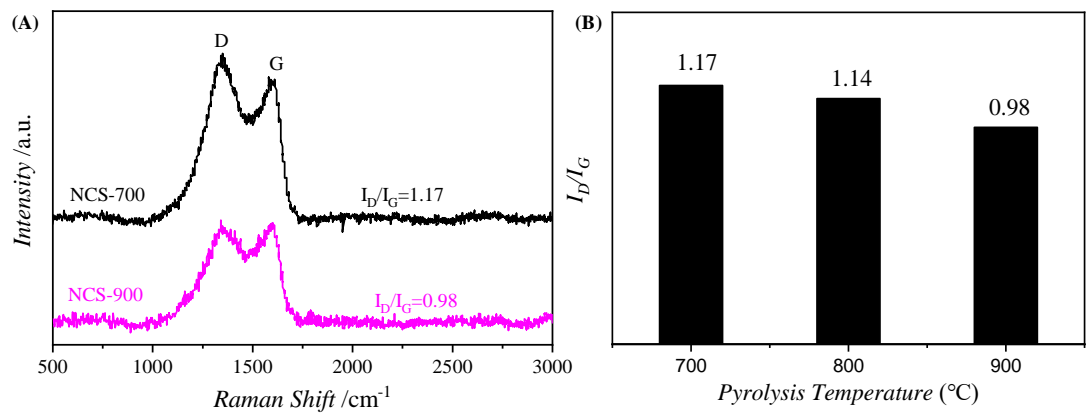


Fig. S18. (A) Raman spectra of NCS-700 and NCS-900, and (B) summary of  $I_D/I_G$  values of NCS-700, NCS-800 and NCS-900.

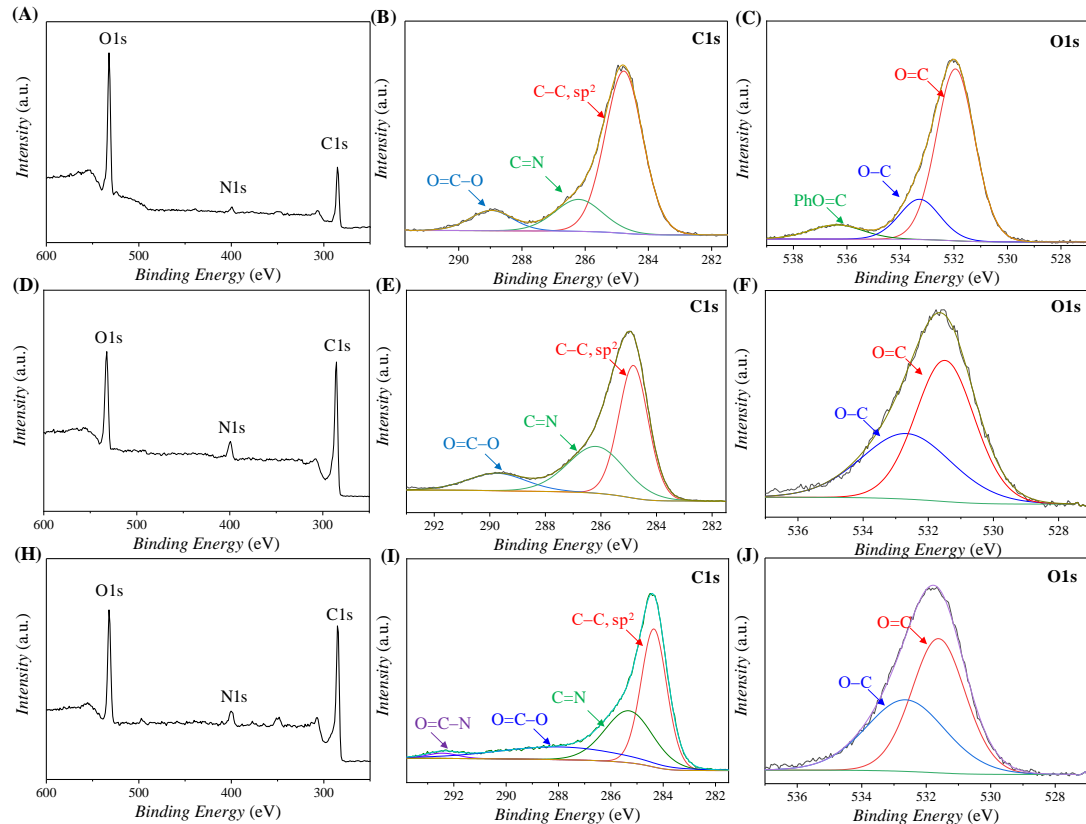


Fig. S19. XPS surveys and high resolution spectra of (A-C) NCS-700, (D-F) NCS-800 and (H-J) NCS-900, respectively.

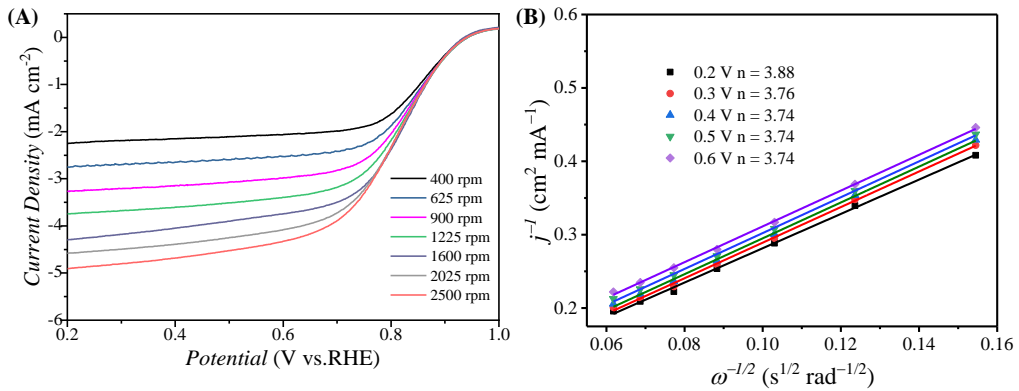


Fig. S20. (A) LSV curves of NCS-800 at different rotation speed and (B) electron transfer number (n) at different potential calculated from Koutechy-Levich (K-L) equation.

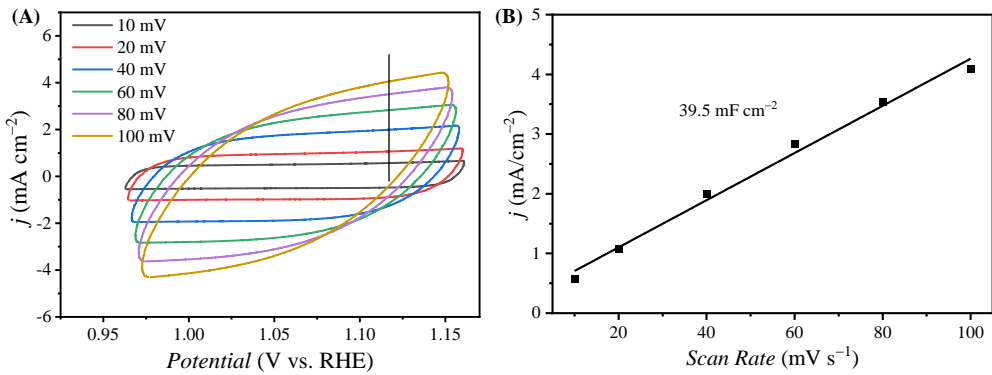


Fig. S21. (A) Cyclic voltammetry (CV) curves at different scan rate and (B) electrochemical double layer capacitance ( $C_{\text{dl}}$ ) of NCS-800.

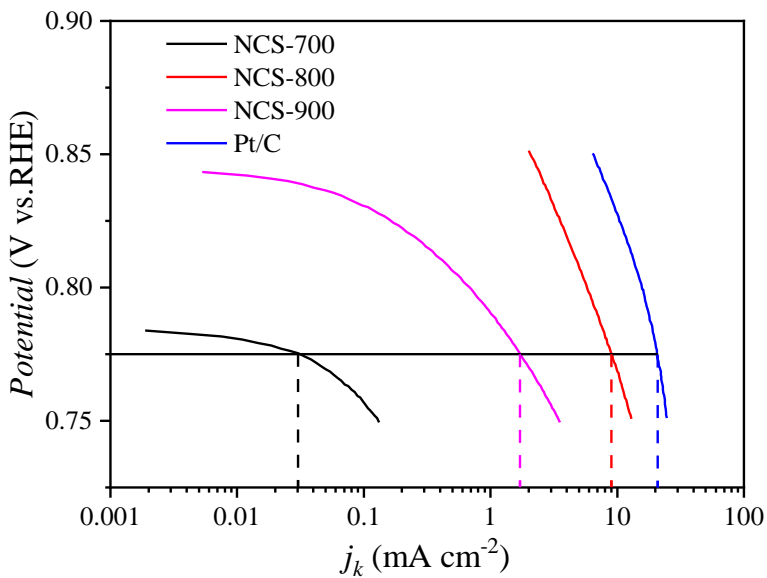


Fig. S22. Tafel plots of NCSs and Pt/C within the potential range of 0.75-0.85 V.

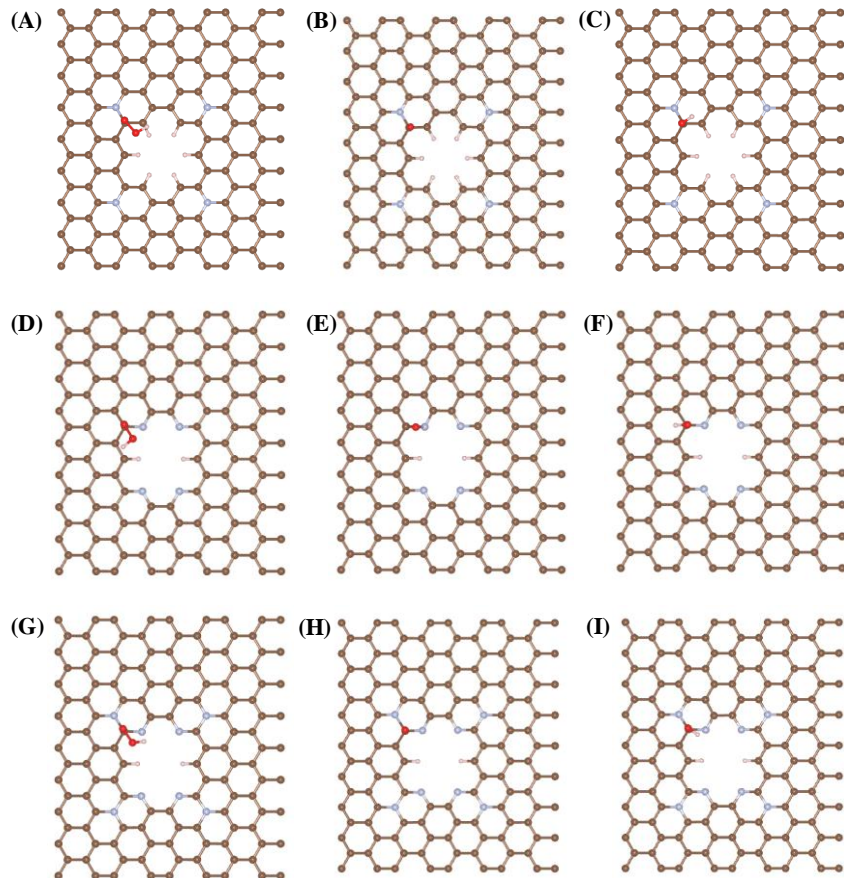


Fig. S23. Optimized configurations of ORR intermediates of (A-C) graphitic N-, (D-F) pyridinic N- and (G-I) graphitic N- and pyridinic N- co-doped carbon.